A physical method for investigating defect chemistry in solid metal oxides

Cite as: APL Mater. 9, 011106 (2021); doi: 10.1063/5.0033891
Submitted: 20 October 2020 • Accepted: 2 January 2021 •
Published Online: 28 January 2021

Christian Rodenbücher,[1,a)] Carsten Korte,[1] Thorsten Schmitz-Kempen,[2] Sebastian Bette,[2] and Kristof Szot[2,3]

AFFILIATIONS

[1] Institute of Energy and Climate Research (IEK-14), Forschungszentrum Jülich GmbH, 52425 Jülich, Germany
[2]aixACCT Systems GmbH, 52068 Aachen, Germany
[3]A. Chełkowski Institute of Physics, University of Silesia, 41-500 Chorzów, Poland

[a)]**Author to whom correspondence should be addressed:** c.rodenbuecher@fz-juelich.de

ABSTRACT

The investigation of the defect chemistry of solid oxides is of central importance for the understanding of redox processes. This can be performed by measuring conductivity as a function of the oxygen partial pressure, which is conventionally established by using buffer gas mixtures or oxygen pumps based on zirconia. However, this approach has some limitations, such as difficulty in regulating oxygen partial pressure in some intermediate-pressure regions or the possibility of influencing the redox process by gases that can also be incorporated into the oxide or react with the surface via heterogeneous catalysis. Herein, we present an alternative physical method in which the oxygen partial pressure is controlled by dosing pure oxygen inside an ultra-high vacuum chamber. To monitor the conductivity of the oxide under investigation, we employ a dedicated four-probe measurement system that relies on the application of a very small AC voltage, in combination with lock-in data acquisition using highly sensitive electrometers, minimizing the electrochemical polarization or electro-reduction and degradation effects. By analyzing the model material $SrTiO_3$, we demonstrate that its characteristic redox behavior can be reproduced in good agreement with the theory when performing simultaneous electrical conductivity relaxation and high-temperature equilibrium conductivity measurements. We show that the use of pure oxygen allows for a direct analysis of the characteristic oxygen dose, which opens up various perspectives for a detailed analysis of the surface chemistry of redox processes.

I. INTRODUCTION

Understanding the defect chemistry of solids is key to modeling and predicting their electrochemical properties. This statement is especially true for solid metal oxides, where the amount of point defects such as oxygen vacancies directly determines the electrochemical behavior. Hence, in recent decades, numerous comprehensive experimental and theoretical studies on the point defect chemistry of solid oxides have been conducted that have led to the development of a variety of technological applications that we nowadays use in daily life.[1,2] Examples can be found in the fields of gas sensors, high-temperature superconductors,[3] solid oxide fuel cells,[4] catalysts,[5] capacitors,[6] batteries,[7] or neuromorphic computers.[8] Since the concentration of point defects in an oxide is directly related to the concentration of charge carriers, one of the most straightforward experimental methods to address the defect structure is to measure the electric conductivity as a function of temperature and oxygen activity.[9,10] Traditionally, this is realized by exposing an oxide to a buffer gas mixture,[11] such as CO/CO_2 or H_2/H_2O. Inert gases such as Ar or N_2 with a small amount of O_2 controlled by zirconia pumps[12,13] are also used. Although these methods allow for precise control of oxygen activity, direct information about the changes in the (non)-stoichiometry of the oxide is limited. Furthermore, there is a drawback that surface reactions could lead to uncontrolled redox reactions, e.g., for $KNbO_3$, it was found that the exposure to CO_2 induces more effective oxidation than the exposure to pure O_2.[14] It has also been found that H_2 can be incorporated into $SrTiO_3$, which could even reverse the effect of previously vacuum-induced reductions.[15]

Here, we present an alternate approach to the investigation of the defect chemistry of oxides using a physical method. The centerpiece of this approach is the replacement of the conventional gas

mixtures by pure oxygen, which is dosed into a vacuum chamber. In this way, the oxygen activity can be directly controlled by varying the total oxygen pressure from the atmospheric pressure down to high vacuum conditions, allowing for a detailed analysis of the redox reactions. Upon oxidation, the dose of the oxygen exposure to the sample can be determined, which is an important quantity for surface science and can be used to obtain information about the exchange reactions at the sample surface.

In order to demonstrate the capabilities of the described method, we present investigations of an $SrTiO_3$ single crystal. $SrTiO_3$ is especially suitable for this purpose, as it has become one of the most intensely investigated model materials for transition metal oxides with perovskite structures.[16–19] We present measurements of the resistance of a single crystal in four-probe geometry as a function of oxygen pressure at various temperatures in the range between 700 °C and 1000 °C. We show that the proposed method offers high reproducibility in conductivity measurements. In a proof of principle approach, we demonstrate that high-temperature equilibrium conductance (HTEC) and electrical conductivity relaxation (ECR) measurements can be performed simultaneously, the results of which are in good qualitative agreement with the expectations.

II. THEORY

The macroscopic redox behavior of $SrTiO_3$ can be described by analyzing the equilibrium point defect concentration for a given temperature and oxygen partial pressure. This has been performed in detail, e.g., by Moos and Härdtl[20] and Denk *et al.*,[21] who elaborated on the defect chemistry of $SrTiO_3$ by carefully determining the equilibrium constants of the reactions between the point defects, as we will discuss briefly in the following. When $SrTiO_3$ is exposed to a reducing environment at moderate temperatures, twofold positively ionized oxygen vacancies $V_O^{\cdot\cdot}$ are the major point defects,

$$O_O^x \rightleftharpoons V_O^{\cdot\cdot} + 2e + \frac{1}{2}O_2. \tag{1}$$

These are charge-compensated by electrons, which thus act as intrinsic donors, which lead to the so-called self-doping effect upon reduction. Accordingly, twofold negatively ionized strontium vacancies serve as intrinsic acceptors whose generation is associated with the segregation of SrO, e.g., as surface islands or as embedded Ruddlesden–Popper phases.[22]

$$Sr_{Sr}^x + O_O^x \rightleftharpoons V_{Sr}'' + V_O^{\cdot\cdot} + SrO. \tag{2}$$

As even nominally undoped $SrTiO_3$ single crystals contain a non-negligible amount of extrinsic acceptors, such as Al, Cu, Fe, K, Mg, or Mn, their contribution to the total defect equilibrium by the generation of holes upon ionization must also be taken into account,[23]

$$A^x \rightleftharpoons A' + h. \tag{3}$$

The concentration of thermally generated electrons and holes in $SrTiO_3$ is very small due to a bandgap of 3.25 eV.[24] Hence, the equilibrium of generation and the recombination of electron–hole pairs are on the far left,

$$\text{nil} \rightleftharpoons e + h. \tag{4}$$

By formulating the laws of mass actions for these four reactions together with the overall charge neutrality condition,

$$n + 2[V_{Sr}''] + [A'] = p + 2[V_O^{\cdot\cdot}], \tag{5}$$

where n is the electron concentration and p is the hole concentration as well as the condition that the sum of neutral and ionized acceptors must be constant,

$$[A] = [A^x] + [A'], \tag{6}$$

an equation system of six equations is generated that can be solved for a given temperature and oxygen activity level. This approach does not consider the presence of interstitials, singly ionized and neutral vacancies, which is regarded as being justified for sufficiently high temperatures.[25] In order to model the unintentional acceptor doping, we assumed an acceptor concentration of $10^{18}/cm^3$. Using the equilibrium constants derived by Moos and Härdtl,[20] which are listed in the supplementary material, we calculated the defect concentration as a function of oxygen (partial) pressure using a computer-algebra software for numerical computing (Maplesoft, Waterloo, Canada). The resulting Kröger–Vink diagram is shown in Fig. 1(a) for a temperature of 1000 °C. The diagrams for the temperatures between 700 °C and 900 °C can be found in the supplementary material.

The calculation predicts that the concentration of oxygen vacancies increases with the decrease in oxygen pressure and that the concentration of strontium vacancies decreases. Below a pressure of 0.8 bar, oxygen vacancies are the majority point defects. Regarding the concentration of electrons and holes, it can be seen that at atmospheric pressure, holes are dominant and that their concentration decreases with the decrease in O_2 partial pressure, whereas the electron concentration increases. Hence, electrons become the dominant charge carriers below an O_2 partial pressure of 10^{-6} bar. In order to illustrate the consequences of the behavior of point defects on the electric characteristic of a solid oxide, we calculated the macroscopic conductivity σ using the derived charge carrier concentration.[20] As the ionic transference number above 500 °C is small, ionic contributions are neglected,[26]

$$\sigma = en\mu_n + ep\mu_p. \tag{7}$$

In Fig. 1(b), it can be seen that the conductivity initially decreases with the decrease in oxygen pressure and then increases again after reaching a minimum. This intrinsic minimum marks the transition from a regime at high O_2 partial pressure, where p-conductivity prevails, to one at low O_2 partial pressure, where n-conductivity is dominant.[27] With the decrease in temperature, the intrinsic minimum shifts to a lower O_2 partial pressure due to the relatively smaller concentration of electrons. As the conductivity is experimentally observable, a direct comparison with the theory can be performed using an HTEC measurement.[28]

When the O_2 partial pressure in the surroundings of a solid oxide is rapidly changed, the material relaxes into a new equilibrium state. As this relaxation process directly relates to the oxygen incorporation, information about the surface exchange and chemical diffusion can be obtained by analyzing the conductivity traces, which are measured during the relaxation process using the ECR method.[29–32] The process of oxygen incorporation must be regarded

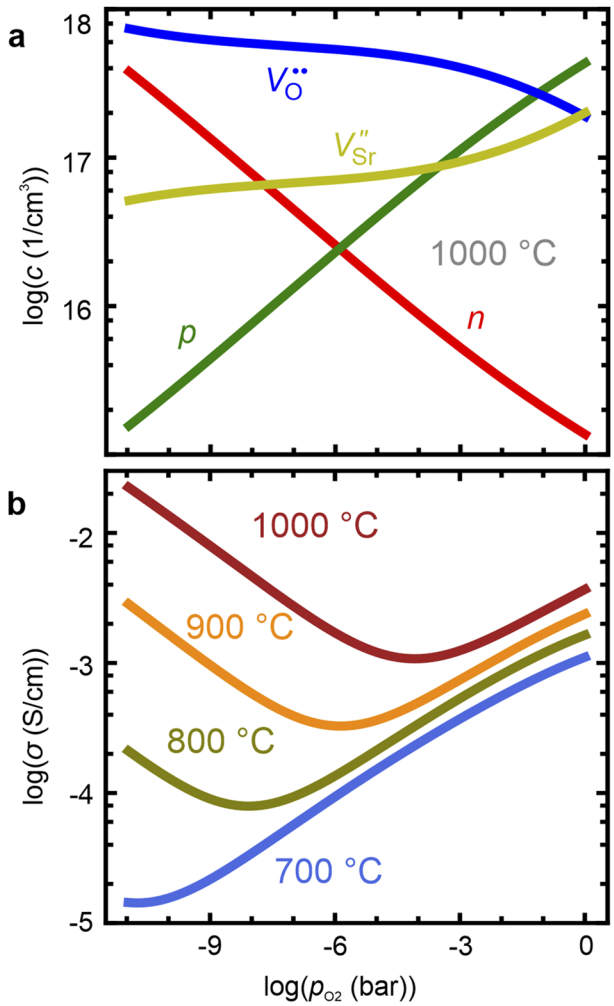

FIG. 1. Point defect chemistry of $SrTiO_3$. (a) Kröger–Vink diagram of defect concentrations calculated for nominally undoped $SrTiO_3$ at a temperature of 1000 °C. (b) Conductivities calculated from the concentration of electrons and holes and their mobilities for different temperatures.

as a two-step one comprising a surface reaction and the diffusion of O^{2-} ions into the bulk.[16] It has been shown by Yasuda and Hishinuma[33] that the oxygen concentration during relaxation can be described by solving Fick's law in three dimensions,

$$\frac{\partial c}{\partial t} = D\nabla^2 c, \tag{8}$$

where c is the oxygen concentration in the oxide, which changes with time t and D is the chemical diffusion coefficient. Again, the model assumes an ideal crystal and does not account for inhomogeneous oxygen transport, which could occur, e.g., along the grain boundaries or dislocations. In this model, the effect of the surface reaction is considered as the boundary condition, following the approach of Crank[34] and introducing the surface exchange coefficient k. The oxygen concentration c is directly related to the normalized conductivity,

$$\tilde{\sigma}(t) = \frac{\sigma(t) - \sigma_0}{\sigma_\infty - \sigma_0}, \tag{9}$$

where σ_0 is the conductivity before the pressure step and σ_∞ is the conductivity in the new equilibrium measured immediately before the next pressure step was initiated. Hence, by performing least-squares fitting of the measured relaxation traces to the solution of Fick's law (see the supplementary material), the parameters k and D can be determined.

III. EXPERIMENTAL SETUP

An aixDCA—Defect Chemistry Analyzer setup built by aixACCT Systems—was used. It consisted of an ultra-high vacuum (UHV) chamber, with a quartz tube at one end, where the sample was positioned, as shown in Fig. 2(a). The tube was surrounded by a temperature-controlled furnace, allowing for the performance of measurements of up to 1000 °C. Using a turbo pump in combination with an oil-sealed rotary pump serving as a backing pump, total pressures down to 10^{-10} bar could be achieved. In order to perform measurements at different oxygen partial pressures, highly purified oxygen with a degree of 6.0 was continuously dosed into the vacuum chamber through a dosing valve (DV). The pressure was controlled using a Bayard–Alpert vacuum gauge[35] in the range of 10^{-10} bar–10^{-6} bar (P_{G1}). The vacuum gauge was calibrated beforehand against a quadrupole mass spectrometer (for details, see the supplementary material). In this way, the oxygen activity in the thermodynamic equilibrium directly corresponds to the recalibrated total pressure measured by using the pressure gauge. As during measurement in this pressure regime, a constant flow of oxygen was present, and dedicated non-flammable oils had to be used in the rotary pump to avoid an explosion. Higher oxygen pressures of between 10^{-6} bar and 1 bar were achieved by closing the shut-off valve (SV) between the vacuum chamber and pump and filling in the oxygen until the desired pressure had been reached. Then, the dosing valve was closed and the measurements were performed in a static atmosphere. To reduce the oxygen pressure again, the shut-off valve was partially opened. This pressure control was performed by manually operating the valves. In the high-pressure regime, capacitance diaphragm gauges (P_{G2}–P_{G3}) were used to measure the pressure.

$SrTiO_3$ single crystals with a size of 10 mm × 4 mm × 1 mm (Shinkosha, Yokohama, Japan) were investigated in a four-probe geometry. Four electrodes were deposited on the top and backside of the crystal using a Pt paste. The distance between the inner electrodes was ~7 mm. Due to the preparation method of the electrodes based on applying the Pt paste by hand, a variation in the distance and shape resulting in a systematic error of the electrode dimensions of ~30% had to be expected. Pt wires wrapped around the crystal were used as electrical connectors, as well as for the mechanical support of the sample, as shown in Fig. 2(b). The electronic measurements were performed by applying an AC voltage at a frequency of 172.5 Hz provided by a generator to the outer electrodes. In order to avoid a potential stoichiometry polarization[36] or charging[37] during the measurement, a small amplitude of 4 mV was used. To measure the current, a current–voltage converter with an amplification

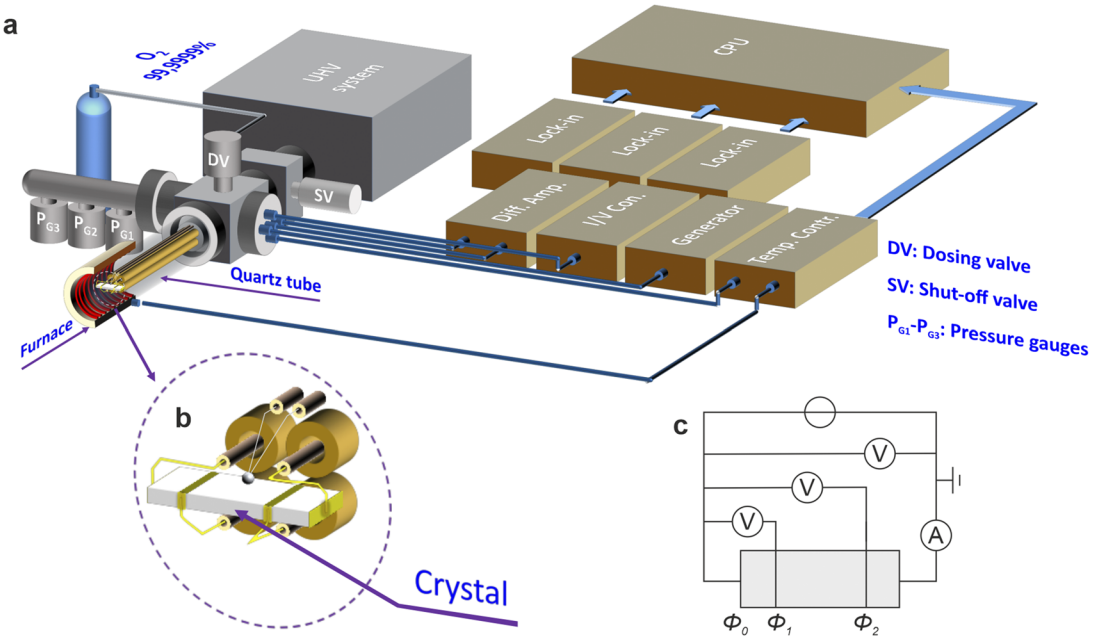

FIG. 2. Illustration of the experimental setup: (a) schematics of the UHV chamber, where the crystal (b) is positioned and contacted in four-probe geometry. (c) The measurement electronics and the schematic circuit diagram.

of 10^5 was employed. The electrical potentials Φ_0, Φ_1, and Φ_2 at three electrodes were measured using sensitive electrometers connected via triaxially screened cables, and one outer electrode was grounded [cf. Fig. 2(c)]. In this way, the voltage drops between the outer electrodes, between inner electrodes, and between the outer and inner electrode on each side of the crystal were recorded via a lock-in technique by a central processing unit (CPU). The total resistance of the sample, the bulk resistance, and the interface resistances were calculated using the rms values of the potentials and the current.

$$R_{total} = \frac{\Phi_0}{I}, \tag{10}$$

$$R_{bulk} = \frac{\Phi_1 - \Phi_2}{I}, \tag{11}$$

$$R_{interface\,1} = \frac{\Phi_0 - \Phi_1}{I}, \tag{12}$$

$$R_{interface2} = \frac{\Phi_2}{I}. \tag{13}$$

Subsequently, the macroscopic conductivity σ was determined using the distance between the electrodes d and the thickness t and width w of the sample,

$$\sigma = \frac{d}{R_{bulk} \cdot t \cdot w}. \tag{14}$$

A detailed description and circuit simulation of the electronic measurement system can be found in the supplementary material.

IV. RESULTS AND DISCUSSION

In order to illustrate the capacity of the measurement system, initially, we present a response of the resistance of the sample on a pressure step. At a temperature of 1000 °C, the sample was equilibrated in a vacuum of 10^{-10} bar, i.e., under maximum reducing conditions. Then, the oxygen pressure in the chamber was increased to 10^{-6} bar for 255 s. Subsequently, the chamber was pumped down to the maximum achievable vacuum again. The total resistance of the investigated $SrTiO_3$ crystal measured during this oxygen exposure is shown in Fig. 3, together with the partial resistances of the bulk and the two interfaces. It can be seen that the resistance of the sample reacted very sensitively and increased immediately upon an increase in the oxygen pressure. After an oxidation time t_{ox} of 190 s, the resistances reached a plateau and remained almost constant until the oxygen was pumped out of the chamber again. As the oxygen pressure during the oxidation was known, we could calculate the oxygen dose D to which the sample was exposed until the new equilibrium was established,

$$D = p_{O_2} \cdot t_{ox} = 1.4 \times 10^5\ \text{L}. \tag{15}$$

Comparing the resistances of the different sample regions, it can be seen that initially, the bulk resistance was higher than the resistances of the interfaces. During the exposure, this relationship was inverted and the increase in the interface resistances was faster than that of the bulk resistance. This shows that the surface of the crystal reacts faster than the bulk upon a change in oxygen activity.

Having demonstrated that we are able to measure the resistance changes in oxidation and reduction, we now focus on a detailed

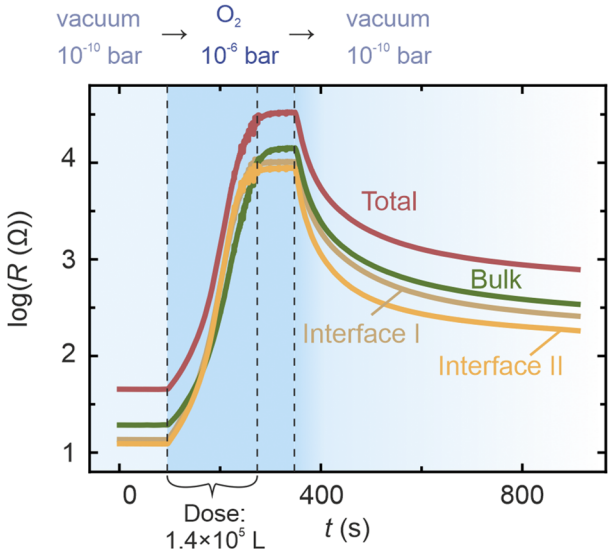

FIG. 3. Resistance response of the $SrTiO_3$ crystal during exposure to 10^{-6} bar oxygen for 255 s at 1000 °C.

investigation of the defect chemistry across the entire accessible oxygen pressure range. We measured the resistance of the crystal while increasing the oxygen pressure in the chamber in a step-wise manner. Before starting the subsequent pressure step, we waited for the establishment of the new equilibrium. In this way, we could obtain ECR and HTEC information simultaneously. In Fig. 4(a), the resistance measurement as a function of time while increasing the oxygen pressure from 10^{-11} to 10^{-1} bar is shown for a temperature of 900 °C. It can be seen that all four resistances reacted similar to the increasing oxygen pressure. The measured bulk resistance was then used to calculate the macroscopic normalized conductivity according to Eqs. (9) and (14), as shown in Fig. 4(b). At low pressures, the equilibration time was in the range of several minutes and decreased significantly to values below 30 s at higher pressures. As shown in detail in the supplementary material, the traces of normalized conductivity for each pressure step were simulated by fitting the solution of the diffusion equation in three dimensions after determining the starting time of each step using the tangent method. Figure 4(c) shows that the simulation agrees satisfactorily with the recorded conductivity data. Here, the pressure step from 1.1 mbar to 5 mbar is shown. The fit depends on two free parameters, namely, the surface exchange coefficient k and the diffusion coefficient D. This dependency is illustrated in the squared error matrix shown in Fig. 4(d). It can be seen that the minimum of the squared error χ is spread out over many orders of magnitude in D. Hence, the simulation is fairly insensitive with D and only a lower limit of 10^{-8} m2/s can be given, whereas the simulation of k is far more reliable. This effect is well known when analyzing ECR data and can potentially be improved in the future by optimizing the sample geometry and experimental conditions.[38–40] The fact that the simulation is more sensitive to the exchange coefficient could also indicate that the surface reaction is the rate determining step,[16] which depends on the morphology

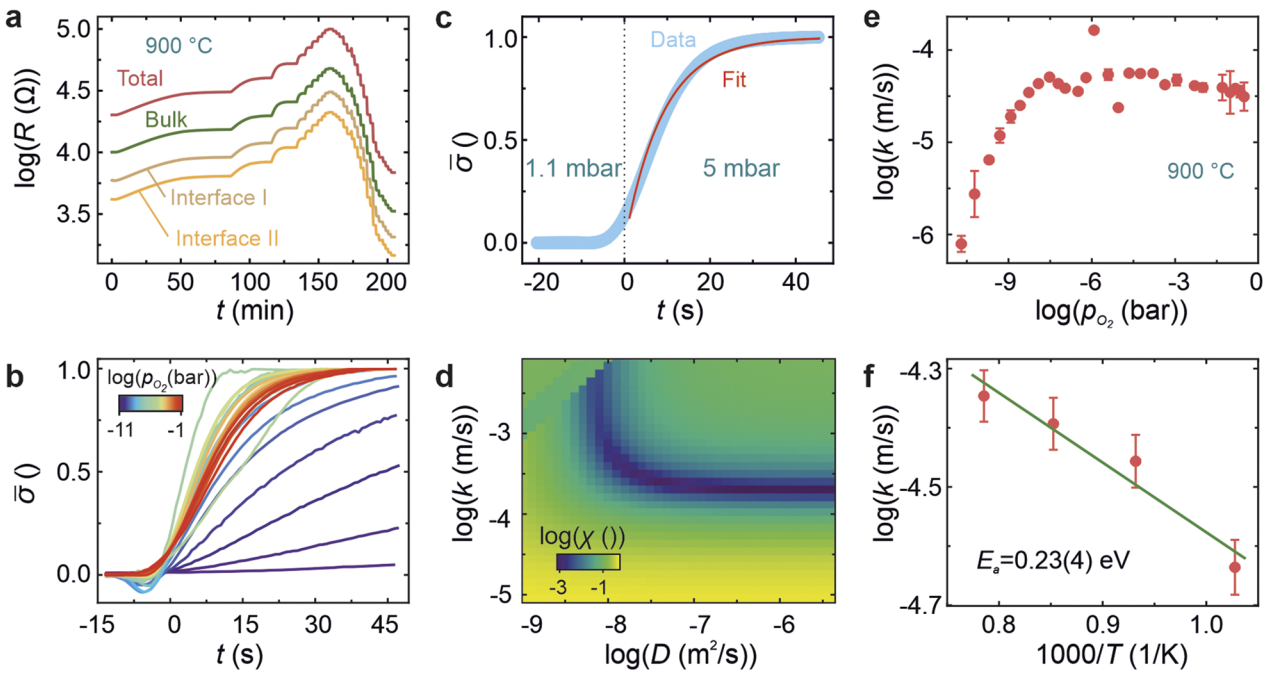

FIG. 4. Electronic conductivity relaxation analysis at 900 °C. (a) Resistance of the sample upon stepwise exposure to oxygen from 10^{-11} to 0.3 bar. (b) Normalized conductivity calculated from the "bulk" data in (a). (c) Comparison between the data and fit shown for the oxygen step from 1.1 mbar to 5 mbar. (d) Squared error matrix of the diffusion coefficient D and the surface exchange coefficient k used for generating the fit in (c). (e) Estimated surface exchange coefficient as a function of the oxygen pressure. (f) Arrhenius plot of the surface exchange coefficient in the high-pressure regime ($p > 10^{-4}$ bar).

and chemical composition of the surface.[41] Figure 4(e) shows the result of the simulation of k at a temperature of 900 °C as a function of the oxygen pressure. In the low pressure regime, k increases with the increase in pressure before staying at the same order of magnitude above a pressure of 10^{-5} bar. Here, it should be kept in mind that the oxygen pressure was established by dosing pure oxygen inside the vacuum chamber. Hence, at low pressure, the mean free path of the oxygen molecules is very large and the decreased surface exchange coefficient may relate to the fact that the transport of oxygen from the vacuum atmosphere to the sample surface slowed down. By analyzing the ECR data of different temperatures between 700 °C and 1000 °C (see the supplementary material), an Arrhenius diagram of k was obtained, as shown in Fig. 4(f). In order to exclude the low pressure data, the mean of k was calculated, taking only values above 10^{-4} bar for each temperature. Using linear regression, an activation energy of the surface exchange reaction of 0.23(4) eV was calculated, which is significantly lower than that obtained by optical studies.[32]

In order to extract the HTEC information from the recorded data, the macroscopic conductivity values were analyzed after reaching an equilibrium for each pressure step. They are plotted as a Brouwer diagram in Fig. 5(a). The data are in good qualitative agreement with the theoretical calculation in Fig. 1(b) and with previous HTEC measurements, which used gas mixtures to establish the oxygen partial pressure. As expected, the $\log(\sigma)/\log(p_{O2})$ plot follows a slope of +1/4 in the high-pressure regime. In the low-pressure one, it tends to approach a slope of −1/4, but not enough data points could be obtained to derive clear evidence of this. By using the conductivity in the intrinsic minimum, where the contribution of holes and electrons to the conductivity is equal, the formation enthalpy of an electron–hole pair and, subsequently, the bandgap energy E_g^0 at T = 0 K can be estimated through an Arrhenius fit,[20] as shown in Fig. 5(b) [cf. Eq. (2) in the supplementary material]. Here, we exclude the measurement performed at 700 °C, as the conductivity minimum could not be clearly identified because it was too close to the lower limit of the achievable O_2 pressure range. In order to calculate the bandgap energy from the slope of the fit, the activation energy of the product of the density of the states in the valence band and the hole mobility was used as calculated by Moos and Härdtl,[20] and the ionic partial conductivities were neglected. We obtain a value of 2.50(2) eV, which is lower than the literature value of the bandgap of 3.25 eV.[24] This difference could relate to the influence of ionic conductivity in the intrinsic minimum. For example, Ohly *et al.*[42] extrapolated the linear fit of the Brouwer diagram in the n and p regions to determine the conductivity in the minimum. We did not compensate for this contribution because a typical plateau close to the intrinsic minimum was not observed. It should also be noted that the bandgap at the surface can be much smaller than that of the bulk. By x-ray photoelectron microscopy (XPS), we were able to find a value of approximately 2.7 eV (see the supplementary material). As it has been found that the surface layer of $SrTiO_3$ plays a dominant role in electrical transport,[43] the deviation in the estimated bandgap from the bulk value may reflect that the macroscopic conductivity is primarily determined by the conductivity of the surface layer.

Similarly, the activation energy in the oxidizing regime was calculated by performing an Arrhenius fit using the conductivity measured at 10^{-1} bar. As shown in Fig. 5(b), an activation energy of E_a^{ox} = 0.42(1) eV is obtained, resulting in an oxidation enthalpy of

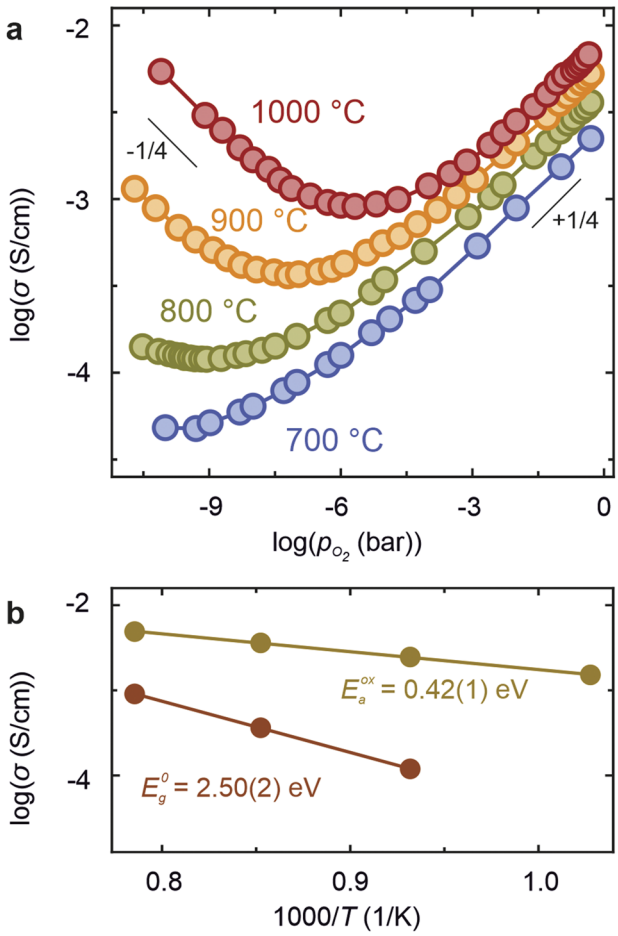

FIG. 5. HTEC analysis of the $SrTiO_3$ crystal at different temperatures. (a) Brouwer diagram of the conductivity as a function of partial pressure. (b) Arrhenius plot of the conductivity in the extrinsic minimum and in the high-pressure regime.

$\Delta H^{ox} = 2E_a^{ox}$ = 0.84(2) eV, which is also slightly lower than in the literature.[20,44] A direct comparison of the Brouwer diagram obtained in this study with literature data can be found in the supplementary material, which shows that our method reproduces the pressure dependence of the conductivity with the comparable data quality. However, a significant variation between the data published in different papers concerning the magnitude of the conductivity and the slopes of the pressure-dependent conductivity curves and the position of the intrinsic minimum is also present.[12,13,20,45,46] Despite these discrepancies, which may be related to a variation in crystal production and preparation[47,48] and could be systematically investigated in the future, our proof-of-concept approach shows that the characteristic Brouwer diagram of $SrTiO_3$ can be reproduced using pure oxygen without the need of buffering gas mixtures. The agreement between the data measured in this study using pure oxygen and previous studies using gas mixtures also confirms that the sample was in thermodynamic equilibrium with the surrounding gas atmosphere during the HTEC measurements (for a detailed comparison, see the supplementary material).

Although we find apparent good agreement between our macroscopic measurement and the theory of point defect chemistry, we would like to note a few caveats relating to the conductivity of $SrTiO_3$, whose detailed investigation lays far beyond the scope of the present paper. Using techniques with a high spatial resolution such as local-conductivity atomic force microscopy (LC-AFM), it has been shown that electronic transport in $SrTiO_3$ is highly inhomogeneous on the nanoscale and that dislocations play a decisive role as easy reduction sites.[48–50] By thermal reduction, it is even possible to induce an insulator-to-metal transition in $SrTiO_3$, i.e., generating a conduction state that lies outside of the Brouwer diagram.[51] These effects may be of particular relevance when building nanoscale devices, such as for resistive switching applications.[52,53]

The possibility of analyzing the point defect chemistry diagrams through the controlled exposure of the clean $SrTiO_3$ surface at precisely defined oxygen doses presented here opens up a new path in the search for a "common denominator" between data obtained through macroscopic electrical characterization and that obtained using surface sensitive experimental methods and theoretical *ab initio* calculations. The local stoichiometry, chemical composition, crystallographic structure (in-plane), electronic structure, local electrical transport phenomena, and the homogeneity of the redox reaction can be analyzed in detail for the definition of the boundary conditions for the reaction surface/gas phase. For instance, it can be shown by XPS studies of the $SrTiO_3$ crystal after different reduction and reoxidation steps that the electronic structure of the surface is significantly changed. Upon thermal reduction, the valences of the Ti ions are partially changed from +4 to +3 and +2 and occupied states in the bandgap evolve, and also, a portion of the oxygen ions can be removed from the crystal.[48] These changes are reversed by reoxidation, showing that the oxygen vacancies are refilled and the charge distribution returns to the initial state (see the supplementary material). Combining these data on the electronic structure with other surface-sensitive techniques such as LC-AFM, low-energy electron diffraction (LEED), or scanning tunneling microscopy (STM), providing information about the atomic arrangement of the surface, models regarding the oxygen exchange reactions can be directly verified and correlated with the measurements of macroscopic conductivity.

V. CONCLUSIONS

In summary, in this study, we have shown that the point defect chemistry of solid metal oxides can be investigated using a typical surface physics method, which relies on exposing the sample to controlled doses of pure O_2 in a vacuum chamber. This method eliminates potential catalytic surface reactions or a significant proton incorporation, which can occur when gas mixtures are used. By measuring the conductivity of $SrTiO_3$ as a function of time and oxygen pressure, the characteristic behavior, as modeled by point defect chemistry, could be reproduced, showing that the method is fully capable of investigating the redox behavior of solid oxides. Using a four-probe measurement technique, in combination with an AC lock-in technique, detailed information about the behavior of the surface region and bulk can be obtained. Although the interface between the Pt electrodes and $SrTiO_3$ crystal shows a different kinetic response than the bulk of the sample, their pressure-dependent defect behavior is the same. Due to the use of pure oxygen, the introduced setup provides extensive information about the oxygen dose, which can help illuminate the surface chemistry, especially concerning the kinetics of the exchange reactions for the bulk and interfaces. As the physical method of investigating defect chemistry introduced here is compatible with other measurement techniques that require UHV conditions such as mass spectrometry, photoelectron spectroscopy, or scanning probe methods, we expect that our approach can help bridge the gap between macro- and nanoscale understanding of electronic transport in transition metal oxides by combining conductivity measurements with *in situ* analytics in the future.

SUPPLEMENTARY MATERIAL

See the supplementary material for details on the theory of point defect chemistry, the electronic measurement system, data processing, ECR simulation, and background information regarding the analysis of $SrTiO_3$ single crystals using surface-sensitive techniques.

ACKNOWLEDGMENTS

We gratefully acknowledge C. Wood for proofreading the manuscript.

DATA AVAILABILITY

The data that support the findings of this study are available from the corresponding author upon reasonable request.

REFERENCES

[1] F. Gunkel, D. V. Christensen, Y. Z. Chen, and N. Pryds, Appl. Phys. Lett. **116**, 120505 (2020).
[2] R. Schmitt, A. Nenning, O. Kraynis, R. Korobko, A. I. Frenkel, I. Lubomirsky, S. M. Haile, and J. L. M. Rupp, Chem. Soc. Rev. **49**, 554 (2020).
[3] M. Quilitz and J. Maier, Radiat. Eff. Defects Solids **137**, 327 (1995).
[4] M. C. Verbraeken, T. Ramos, K. Agersted, Q. Ma, C. D. Savaniu, B. R. Sudireddy, J. T. S. Irvine, P. Holtappels, and F. Tietz, RSC Adv. **5**, 1168 (2015).
[5] P. Hartmann, T. Brezesinski, J. Sann, A. Lotnyk, J.-P. Eufinger, L. Kienle, and J. Janek, ACS Nano **7**, 2999 (2013).
[6] M. Höfling, S. Steiner, A.-P. Hoang, I.-T. Seo, and T. Frömling, J. Mater. Chem. C **6**, 4769 (2018).
[7] J. Maier, J. Electrochem. Soc. **162**, A2380 (2015).
[8] M. Lübben, F. Cüppers, J. Mohr, M. von Witzleben, U. Breuer, R. Waser, C. Neumann, and I. Valov, Sci. Adv. **6**, eaaz9079 (2020).
[9] M. K. Nowotny, T. Bak, and J. Nowotny, J. Phys. Chem. B **110**, 16270 (2006).
[10] P. Kofstad, *High-Temperature Oxidation of Metals* (John Wiley & Sons, 1966).
[11] S. Steinsvik, R. Bugge, J. Gjønnes, J. Taftø, and T. Norby, J. Phys. Chem. Solids **58**, 969 (1997).
[12] C. Ohly, S. Hoffmann-Eifert, X. Guo, J. Schubert, and R. Waser, J. Am. Ceram. Soc. **89**, 2845 (2006).
[13] X.-D. Zhang, J.-J. Li, and X. Guo, Rev. Sci. Instrum. **86**, 115103 (2015).
[14] K. Szot, J. Keppels, W. Speier, K. Besocke, M. Teske, and W. Eberhardt, Surf. Sci. **280**, 179 (1993).
[15] B. Jalan, R. Engel-Herbert, T. E. Mates, and S. Stemmer, Appl. Phys. Lett. **93**, 052907 (2008).
[16] R. Merkle and J. Maier, Angew. Chem., Int. Ed. **47**, 3874 (2008).
[17] L. Amaral, A. Tkach, P. M. Vilarinho, and A. M. R. Senos, J. Phys. Chem. C **123**, 710 (2019).
[18] R. Waser, J. Am. Ceram. Soc. **74**, 1934 (1991).

[19]G. Scheerer, M. Boselli, D. Pulmannova, C. W. Rischau, A. Waelchli, S. Gariglio, E. Giannini, D. van der Marel, and J.-M. Triscone, Condens. Matter **5**, 60 (2020).
[20]R. Moos and K. H. Härdtl, J. Am. Ceram. Soc. **80**, 2549 (1997).
[21]I. Denk, W. Münch, and J. Maier, J. Am. Ceram. Soc. **78**, 3265 (1995).
[22]K. Szot and W. Speier, Phys. Rev. B **60**, 5909 (1999).
[23]P. C. Bowes, J. N. Baker, and D. L. Irving, J. Am. Ceram. Soc. **103**, 1156 (2020).
[24]K. van Benthem, C. Elsässer, and R. H. French, J. Appl. Phys. **90**, 6156 (2001).
[25]R. Moos and K. H. Härdtl, J. Appl. Phys. **80**, 393 (1996).
[26]R. A. Maier and C. A. Randall, J. Am. Ceram. Soc. **99**, 3350 (2016).
[27]R. Moos and K. H. Hardtl, J. Am. Ceram. Soc. **78**, 2569 (1995).
[28]F. Gunkel, S. Hoffmann-Eifert, R. Dittmann, S. B. Mi, C. L. Jia, P. Meuffels, and R. Waser, Appl. Phys. Lett. **97**, 012103 (2010).
[29]I. Yasuda, J. Electrochem. Soc. **141**, 1268 (1994).
[30]J. Lane and J. A. Kilner, Solid State Ionics **136-137**, 997 (2000).
[31]Y. Li, K. Gerdes, H. Diamond, and X. Liu, Solid State Ionics **204-205**, 104 (2011).
[32]K. Kerman, C. Ko, and S. Ramanathan, Phys. Chem. Chem. Phys. **14**, 11953 (2012).
[33]I. Yasuda and M. Hishinuma, J. Solid State Chem. **123**, 382 (1996).
[34]J. Crank, *The Mathematics of Diffusion*, 2d ed. (Clarendon Press, Oxford [Eng], 1975).
[35]R. Silva, N. Bundaleski, A. L. Fonseca, and O. M. N. D. Teodoro, Vacuum **164**, 300 (2019).
[36]C. Rodenbücher, P. Meuffels, G. Bihlmayer, W. Speier, H. Du, A. Schwedt, U. Breuer, C.-L. Jia, J. Mayer, R. Waser, and K. Szot, Sci. Rep. **8**, 3774 (2018).
[37]I. Valov, E. Linn, S. Tappertzhofen, S. Schmelzer, J. van den Hurk, F. Lentz, and R. Waser, Nat. Commun. **4**, 1771 (2013).
[38]F. Ciucci, Solid State Ionics **239**, 28 (2013).
[39]E. Fischer and J. L. Hertz, Solid State Ionics **218**, 18 (2012).
[40]K. J. Skaja, *Redox Processes and Ionic Transport in Resistive Switching Binary Metal Oxides* (RWTH Aachen University, 2016).
[41]D. Wrana, C. Rodenbücher, W. Bełza, K. Szot, and F. Krok, Appl. Surf. Sci. **432**, 46 (2018).
[42]C. Ohly, S. Hoffmann-Eifert, K. Szot, and R. Waser, J. Eur. Ceram. Soc. **21**, 1673 (2001).
[43]A. Leis, C. Rodenbücher, K. Szot, V. Cherepanov, F. S. Tautz, and B. Voigtländer, Sci. Rep. **9**, 2476 (2019).
[44]G. M. Choi and H. L. Tuller, J. Am. Ceram. Soc. **71**, 201 (1988).
[45]N. H. Chan, R. K. Sharma, and D. M. Smyth, J. Electrochem. Soc. **128**, 1762 (1981).
[46]W. Menesklou, H.-J. Schreiner, K. H. Härdtl, and E. Ivers-Tiffée, Sens. Actuators, B **59**, 184 (1999).
[47]C. Rodenbücher, M. Luysberg, A. Schwedt, V. Havel, F. Gunkel, J. Mayer, and R. Waser, Sci. Rep. **6**, 32250 (2016).
[48]K. Szot, C. Rodenbücher, G. Bihlmayer, W. Speier, R. Ishikawa, N. Shibata, and Y. Ikuhara, Crystals **8**, 241 (2018).
[49]D. Marrocchelli, L. Sun, and B. Yildiz, J. Am. Chem. Soc. **137**, 4735 (2015).
[50]C. Rodenbücher, D. Wrana, T. Gensch, F. Krok, C. Korte, and K. Szot, Crystals **10**, 665 (2020).
[51]K. Szot and C. Rodenbücher, in *2015 Joint IEEE International Symposium on Applications of Ferroelectric (ISAF), International Symposium on Integrated Functionalities (ISIF) Piezoresponse Force Microscopy Workshop (PFM)* (IEEE, 2015), p. 143.
[52]K. Szot, W. Speier, G. Bihlmayer, and R. Waser, Nat. Mater. **5**, 312 (2006).
[53]D. H. Kwon, S. Lee, C. S. Kang, Y. S. Choi, S. J. Kang, H. L. Cho, W. Sohn, J. Jo, S. Y. Lee, K. H. Oh, T. W. Noh, R. A. De Souza, M. Martin, and M. Kim, Adv. Mater. **31**, 1901322 (2019).